Atmos. Meas. Tech. Discuss., 6, 8187–8233, 2013
www.atmos-meas-tech-discuss.net/6/8187/2013/
doi:10.5194/amtd-6-8187-2013

Atmospheric Measurement Techniques
Discussions
Open Access

CloudSat-constrained cloud ice water path and cloud top height retrievals from MHS 157 and 183.3 GHz radiances

J. Gong[1,2] **and D. L. Wu**[2]

[1]University Space Research Association, Columbia, MD, USA
[2]Climate and Radiation Branch, MC 613.2, NASA/Goddard Space Flight Center, Greenbelt, MD, USA

Received: 29 May 2013 – Accepted: 28 August 2013 – Published: 4 September 2013

Correspondence to: J. Gong (jie.gong@nasa.gov)

Published by Copernicus Publications on behalf of the European Geosciences Union.

Abstract

Ice water path (IWP) and cloud top height (h_t) are two of the key variables to determine cloud radiative and thermodynamical properties in the climate models. Large uncertainty remains among IWP measurements from satellite sensors, in large part due to the assumptions made for cloud microphysics in these retrievals. In this study, we develop a fast algorithm to retrieve IWP from the 157, 183.3 ± 3 and 190.3 GHz radiances of Microwave Humidity Sounder (MHS) such that the MHS cloud ice retrieval is consistent with CloudSat IWP measurements. This retrieval is obtained by constraining the forward models between collocated-and-coincident measurements of CloudSat IWP and MHS cloud-induced radiance depression (T_{cir}) at these channels. The empirical forward model is represented by a look-up-table (LUT) of T_{cir}–IWP relationships as a function of h_t and frequency channel. With h_t simultaneously retrieved, the IWP is found to be more accurate. The useful range of the MHS IWP retrieval is between 0.5 and 10 kg m^{-2}, and agrees well with CloudSat in terms of normalized probability density function (PDF). Compared to the empirical model, current radiative transfer models (RTMs) still have significant uncertainties in characterizing the observed T_{cir}–IWP relationships. Therefore, the empirical LUT method developed here remains as an effective approach to retrieving ice cloud properties from the MHS-like microwave channels.

1 Introduction

Ice clouds have profound impacts on the global energy budget Stephens et al. (1990), hydrological cycle (Chahine, 1992), atmospheric structure (Ramaswamy and Ramanathan, 1989) and circulation (Richter and Rasch, 2008). Cloud ice water amount is one of the largest sources of uncertainty in quantifying cloud-climate feedbacks and sensitivities. For example, the mean cloud ice water path (IWP) ranges from 10 to 120 g m^2 in the tropics among a variety of Global Climate Models (GCMs) in the most recent 20th century Coupled Model Intercomparison Project Phase 5 (CMIP5) runs (Li et al., 2012). Accurate cloud IWP measurements are critically needed to guide model developments and reduce model uncertainties.

Yet, observations of cloud ice have not met the requirement by climate models, showing several folds of IWP differences among various techniques (Wu et al., 2009; Eliasson et al., 2011). Until cross-instrument consistency is achieved, current cloud ice observations allow too much variation in cloud properties and become insufficient to constrain the model physics (Waliser et al., 2009; Li et al., 2012). Difficulties for accurate IWP and microphysical measurements arise mainly from remote sensing in the presence of cloud inhomogeneity and sensitivity limitations associated with each technique. On one hand, large spatial and temporal variabilities in cloud microphysics make it difficult to compare ground-based measurements with remote sensing observations (Waliser et al., 2009). Hence, statistical representations of cloud microphysics are assumed or parameterized in order to enable satellite remote sensing (e.g., McFarquhar and Heymsfield, 1997). Even for simple optically-thin cloud, there are still great deal of uncertainties in the assumption made for the IWP retrieval. On the other hand, passive satellite sensors have limited penetration capability to observe thick and dense ice clouds from space. As a result, only partial column of IWP (pIWP) can be measured by passive sensors, and the column bottom varies with atmospheric absorption, cloud amount, droplet size and phase, and cloud top height. These uncertainties about cloud column create additional errors in the IWP retrieval using passive sensors.

As an active sensor, CloudSat radar provides an unprecedented opportunity to measure the ice water content (IWC) profile and its vertical integral (i.e., IWP) globally since 2006. The CloudSat cloud ice retrieval still depends on the cloud microphysics constrained by in-situ and ground-based observations (Austin et al., 2009). CloudSat data are confined in a narrow curtain (∼ 1 km width) along the orbital track, and thus are used mostly for climatological and case studies. Like other A-train Sun-synchronous satellites, it samples only two Local Solar Times (01:30 and 13:30 LST) of the cloud diurnal cycle. However, CloudSat data still provides the best characterization of vertical distribution of global cloud ice (Eliasson et al., 2011), and can be used to cross-calibrate other techniques, especially the passive sensors with limited vertical resolution (Wu et al., 2009).

Passive nadir-viewing microwave techniques such as Advanced Microwave Sounding Unit-B (AMSU-B) and Microwave Humidity Sensor (MHS) have advantage over infrared/visible sensors for penetrating deeper into cloud layers to measure IWP. More importantly, MHS has a swath width of ∼ 2300 km to capture synoptic-mesoscale systems in motion as well as variabilities not captured from the curtain-only sampling by CloudSat. Instead of slicing a single vertical cross-section of a hurricane, the entire cyclonic structure can be mapped out with one MHS orbit. Since 1998, satellites carrying the instruments like AMSU-B and MHS have been operational and now flying across the equator at more than eight local solar times everyday, the mosaic of which can be used for cloud diurnal cycle studies. Moreover, at microwave frequencies ice scattering signals are approximately linearly proportional to cloud ice amount in the path, resulting in a relatively straightforward relationship between IWP and cloud-induced radiance depression (Wu et al., 2009). These advantages make nadir-viewing microwave sensors attractive for monitoring global long-term IWP.

Retrieval of IWP requires radiative transfer models (RTMs) or forward models that relate the measured radiance to cloud ice. The cloud ice RTM can be formulated either theoretically or empirically. RTMs are also widely used in climate models but primarily for calculating clear-sky radiative forcing from atmosphere gas, cloud, aerosol and surface. Although studies demonstrated the use of RTMs for IWP retrievals from AMSU-B/MHS channels, considerable uncertainties exist with RTMs in representing complex physical processes (e.g., land surface radiative fluxes, ice particle shape) and with oversimplified assumptions (e.g., plane-parellel atmosphere and cloud layers, cloud droplet size distribution, etc.). The errors in liquid drop size, surface emission/scattering, cloud layer height, and water vapor amount can all degrade the quality of the retrieved IWP. For example, the current operational IWP retrieval algorithm from Microwave Surface and Precipitation Products System (MSPPS), which is based upon a two- stream approximated radiative model solutions (Zhao and Weng, 2002) at

AMSU-B 89 and 150 GHz channels, was found to under-estimate IWP in comparison with other observations (Wu et al., 2009; Waliser et al., 2009; Eliasson et al., 2011; Chen et al., 2011). Contamination of cloud ice retrievals was also found over snowy/icy surfaces (Wu et al., 2009).

While further improvements are still needed for ice scattering calculation in the microwave RTMs, empirical forward models have been used for cloud retrievals (Holl et al., 2010). Empirical approaches establish some ad-hoc relationships between cloud ice variables and radiance/reflectivity measurements from the data themselves. Such empirical forward models are developed from a finite ensemble of observations, and are therefore limited to specific conditions, environments and dynamic ranges of the cloud variable of interest. The algorithms are usually fast in form of look-up table (LUT) and bypass the complex microphysical calculation in cloudy-sky radiative transfer on individual cases. Empirical methods have been also used in surface remote sensing where land properties are too complicated to be modeled or validated (e.g., Pulliainen and Hallikainen, 2001).

In this paper, we develop an empirical model and retrieval algorithms for IWP using cloud-induced radiance depression (T_{cir}) from MHS at 157, 183.3 ± 3 and 190.3 GHz. The empirical forward model is obtained by regressing MHS T_{cir} radiances on collocated CloudSat IWP and cloud top height measurements in the tropics. The sequential estimation method is then used to retrieve IWP for all MHS footprints. The instruments and methodology will be described in Sect. 2, following by the detailed retrieval algorithm in Sect. 3. An evaluation of the retrieved products is given in Sect. 4 with comparisons to the operational product and other RTM results, followed by the summary in Sect. 5.

2 Instruments, data, and methods

2.1 Description of datasets and models

The datasets used in this study are Level-1 brightness temperature (T_B) from MHS, ice water content (IWC) from CloudSat, and Modern Era Retrospective-Analysis for Research and Applications (MERRA) 3-hourly analysis variables on a $1.25^\circ \times 1.25^\circ$ latitude-longitude grid. Two radiative transfer models are used in this study are Joint Center for Satellite Data Assimilation (JCSDA) Community RTM (CRTM) and an ice scattering Cloud Radiance Model (CRM).

2.1.1 MHS T_B, IWP and historical issues

MHS is a cross-track scanning radiometer aboard the National Oceanic and Atmospheric Administration (NOAA) satellite 18, 19, European Organisation for the Exploitation of Meteorological Satellites (EUMETSAT) Metop-A, and B, which is a slightly improved version of AMSU-B onboard NOAA-15, 16, and 17. MHS makes 90- footprints (with a beamwidth of 1.1°) continuously in each cross-track scan and the outmost scan-angle is ±48.95° from nadir. For NOAA-18, the MHS scan and satellite orbital altitude produce a nadir footprint size of 16 km at half power field-of-view (FOV) and a swath width of 2200 km. The FOV size and swath vary slightly among satellites due to different orbital altitudes. MHS has five microwave channels, which are 89, 157, 183.3 ± 1, 183.3 ± 3 and 190.3 GHz (for AMSU-B, the second and last channels are 150 and 183.3 ± 7 GHz, respectively). For consistency, these channels are labeled as CH#1-5 hereafter. MHS CH#1, 2 and 5 are vertically polarized, and the other two are horizontally polarized (for AMSU-B, all five channels are vertically polarized). The designed radiometric noises ($NE\Delta T$) for CH#1–5 are 0.22, 0.34, 0.51, 0.40, and 0.46 K, respectively John et al., 2012. The 89 and 157 GHz are window channels, and those around 183.3 GHz water vapor absorption line are designed to profiling the atmospheric water vapor. Under clear-sky condition, the peak sensitivity of these 183.3 GHz channels occurs in the upper, middle and lower troposphere, respectively. NOAA-15, 16, 17, 18 and 19 orbits drift slowly with time, while Metop-A and B are maintained at a sun-synchronous orbit with fixed Equator Passing Time (EPT).

For ice particle scattering measurement, the higher-frequency channels (157, 183.3 and 190.3 GHz) work better for IWP retrievals because the Mie scattering is proportional to frequency to the fourth power. Scattering-based microwave cloud remote sensing has some unique properties as well as limitations. First, it penetrates deeper into ice clouds than IR and visible techniques for cloud ice measurements, but can become saturated for very optically-thick clouds Seo and Liu, 2006; Arriaga, 2000. In the case of saturation, only partial cloud ice column pIWP can be retrieved. As shown in Seo and Liu (2006), the window channels near 183.3 GHz can penetrate a cloud-layer with IWP as large as 10 $\mathrm{kg\,m^{-2}}$, which covers most of the IWP values observed by CloudSat. However, in the case of graupels, or frontal astrostratus clouds, saturation may occur (Arriaga, 2000). Saturation is also more prominent in the oblique views than nadir (where the line-of-sight path is longer).

Secondly, among all MHS/AMSU-B channels, CH#3 is most sensitive to water vapor because it is adjacent to the 183.3 GHz water vapor absorption line. The absorption from upper tropospheric water vapor, so-called “water vapor screening”, prevents CH#3 from seeing the surface and clouds in the lower troposphere. To some extent, CH#4 has a quite amount of water vapor screening and can observe some ice clouds but remains little contaminated by the surface unless at dry, high latitudes. In other words, CH#4 can be used to distinguish between surface and cloud in the situation where other channels have difficulties, as will be shown in Sect. 2.1.3.

Lastly, microwave radiances are dependent on scan angle at these frequencies. Under clear-sky condition, the radiance may decrease with scan angle from nadir, as a function of the cosine of angle, due to the increasing path length at line-of-sight (LOS). This is similar to the 6.7 µm IR channel where the longer LOS path gives a weighting function at a higher altitude, or cold temperature (Soden, 1998). Under the cloudy-sky condition, the radiance scan-dependence may vary with cloud inhomogeneity as

Title Page
Abstract | Introduction
Conclusions | References
Tables | Figures
◀| |▶
◀ ▶
Back | Close
Full Screen / Esc
Printer-friendly Version
Interactive Discussion

cloud size and distribution are often not homogeneous. In addition to the atmosphere-induced scan angle dependence, there are some instrument errors in all five channels that are scan-dependent and asymmetric about nadir. These instrumental errors can severely degrade quality of the retrieved IWP if not properly corrected. For example, there was a radio-frequency interference (RFI) problem in CH#3 and 4 of AMSU-B (Atkinson, 2001; Buehler et al., 2005), and gain variations/degredations are found in CH#3–5 of AMSU-B on NOAA-16 and 17 (John et al., 2013). MHS exhibits smaller scan-dependent biases than AMSU-B, but suspicious behaviors have been reported for CH#3 on NOAA-18, 19 and Metop-A (John et al., 2013). The MHS instruments on NOAA-18 and Metop-A have so far shown the best overall radiometric calibration for all five channels. Since NOAA-18 has the closest EPT with CloudSat, it is used in this study to develop the cloud ice retrieval constrained by CloudSat. The radiances from CH#3 are not used because they are relatively noisier and provide little information on cloud ice. As in the main weather prediction centers, we use Advanced Television and Infrared Observational Satellite Operational Vertical Sounder (ATOVS) and Advanced Very High Resolution Radiometer (AVHRR) pre-processing Package (AAPP, v7) developed by Numerical Weather Prediction Satellite Application Facilities (NWP SAF) to process the L1B radiance data to obtain the further quality-controlled and calibrated L1C data. In the NOAA-18 MHS L1C data we have not found any systematic instrumental error.

Weng et al. (2003) developed an algorithm to retrieve the IWP using ice scattering at 89 and 150 GHz, which is known as the NOAA operational IWP product. Their retrieval algorithm yields effective ice particle size and IWP with cloud top and base temperatures derived from simultaneous AMSU-A channels. A considerable fraction of false cloud detection was found with this method, mostly over icy/snowy surface and on elevated topography (Wu et al., 2009). The NOAA IWP has been reported to have significantly low values compared with radar and IR measurements (Holl et al., 2010; Eliasson et al., 2011). As an extended product, rain rate is derived from the retrieved IWP with an empirical polynomial relationship (Zhao and Weng, 2002). The operational

NOAA IWP data, now integrated into the MSPPS in the CLASS website, will also be used in this study for comparisons.

2.1.2 CloudSat IWC

Launched to the A-train in April 2006, CloudSat has a 94 GHz Cloud Profiling Radar (CPR) to provide continuous cloud profiles along its nadir track. A CPR FOV size is 1.3 × 1.7 km. Cloud ice water content (IWC) product from 2B-CWC-RO (R04) is used in this study, which assumes a Gamma size distribution of cloud ice particles. The CloudSat IWC retrieval is limited when temperature is above 0 °C, so is the liquid water content (LWC) retrieval at temperatures below −20 °C. Between 0 and −20 °C, IWC and LWC are retrieved separately and linearly interpolated to the intermediate temperature range (details of the algorithm can be found in Austin et al., 2009). Thus, large uncertainties are expected for this mixed-phase cloud regime, and/or in the ice cloud cases with large snow/graupel particles present. The vertical resolution of IWC profile is 250 m. In our study, we interpolate it vertically to an evenly spaced grid (250 m resolution), and integrate the IWC between surface and 19 km to compute the total IWP. We also integrate the IWC profile from different bottom heights to better represent the pIWPs measured by MHS channels. Compared with Holl et al. (2010), who used the CloudSat total column IWP product, our IWC integration approach is more meaningful to compare with pIWP seen from MHS water vapor channels, although the pIWP value is calculated on a profile-by-profile basis. Hereafter, we use IWP as the abbreviation of pIWP in our study to represent MHS cloud ice column.

CloudSat IWC has been validated with in-situ, ground based and other satellite IWC measurements (e.g., Austin et al., 2009; Wu et al., 2009; Protat et al., 2009). The uncertainty is claimed up to 40 % (Austin et al., 2009), which is much smaller than the divergences among various satellites and models, the latter of which often exceed 100 % (Waliser et al., 2009; Eliasson et al., 2011). In this study, we treat CloudSat IWP as the "truth" to constrain the retrieved MHS IWP difference relative to that of CloudSat. Moreover, since microwave penetrates much deeper into ice clouds than IR/VIS channels, we expect our CloudSat-constrained algorithm to yield a better retrieval at large IWP values.

2.1.3 Radiative Transfer Models (RTMs) and computation of T_{cir}

It is the first step in cloud ice retrieval to determine ice cloud induced brightness temperature T_{cir} from raw radiance measurements (Wu et al., 2009, 2013). In this study, T_{cir} is defined as the difference between the measured radiance, T_{B}, and modeled clear-sky background, T_{ccr}:

$$T_{\mathrm{cir}} \equiv T_{\mathrm{B}} - T_{\mathrm{ccr}}. \tag{1}$$

T_{cir} also serves a critical variable for cloud detection since every measurement has an uncertainty that may lead to false alarm. T_{cir} error is largely affected by uncertainty in the estimated T_{ccr}. Various methods have been developed to improve the accuracy of T_{ccr} estimation. Generally speaking, T_{ccr} can be obtained using statistically differences between cloudy and clear skies (Wu et al., 2005), or using radiative transfer model to estimate the clear-sky background from the current atmospheric state. Here we use the second approach with the best estimate of local atmospheric sate variables (e.g., temperature, pressure, water vapor, ozone) and surface conditions (e.g., surface temperature, surface type) from MERRA 3-hourly assimilation dataset from interpolation of adjacent grid points and closest local time. We allow relative humidity to exceed 100 % in computing clear-sky radiation. We also used the MERRA 6-hourly finer-grid analysis product and European Re-Analysis Interim (ERA-Interim) data, but no significant difference of T_{ccr} is found among the results so far in the tropics and subtropics.

The JCSDA CRTM v2.0.5 model is employed to calculate T_{ccr}. CRTM is a fast radiative transfer model that uses advanced doubling-adding method (Liu and Weng, 2006) to compute the radiances and radiance Jacobians at the top-of-atmosphere for various instruments with wavelengths ranging from visible to submilimeter. It includes scattering calculations for cloud, aerosol, gas molecular and surface if specified. As the key backbone of data assimilation (DA) systems, the CRTM has incorporated most space-born instrument information (e.g., spectral frequency, filter shape, and scan pattern), including AMSU-B and MHS. Therefore, it is also our objective to calibrate our cloud ice retrieval with this widely-used CRTM for T_{ccr} estimation so that the IWP outputs can be readily for the DA applications.

Figure 1 presents the probability density functions (PDFs) of T_{cir}, T_{ccr} and TB from a month worth of MHS nadir measurements in the tropics. Warmer TB values are mostly from clear-sky surface, while colder TB are the cases of ice clouds or snow/icy surfaces at a high elevation. The TB PDFs all have a broad peak with a standard deviation (σ) that is so wide that the empirical 3σ cloud detection method (i.e., $TB_{peak} - 3\sigma < 0$ for cloud detection) used by many previous studies does not work well when applied directly to the TB data (e.g., McNally et al., 2006; Gong and Wu, 2013). On the other hand, the T_{ccr} PDFs have a smaller standard deviation because the CRTM-derived T_{ccr} from MERRA data has removed a lot of clear-sky variability (Fig. 1a). The long PDF tail in the negative T_{cir} values is a distribution of cloudy radiances. Ideally, a perfect T_{ccr} model with perfect clear-sky input would produce a singular peak in the T_{cir} PDF at 0 K, and all negative values would be classified as clouds. The uncertainty of T_{cir} measurements, close to a Gaussian distribution, is reflected in the PDF spread near zero, especially on the positive half of the PDF. The ability of separating between cloudy and clear radiances is characterized by this standard deviation σ, which can be computed from this portion of PDF.

However, the CRTM does not always improve cloud detection. For example, the width of CH#2 T_{cir} PDF is not much narrower than that of TB, indicating limited skills of the CRTM in capturing the clear-sky variability. Large error of the calculated T_{ccr} is found over mountains and arid areas where it remains challenging for the CRTM to model surface contributions at CH#2. When excluding all land cases, the CH#2 T_{cir} can produce a PDF with a narrower width around zero (not shown). On average, the T_{cir} error is ∼ 5 K, although it may vary from 7.5 to 10 K. In the cloud ice retrieval later on, the generic value of 5 K is used for all channels. In addition to T_{cir} standard deviation, we also calculate T_{cir} bias for each MHS channel since the clear-sky PDF should peak at zero. We find that the CRTM has a cold bias (∼ 2 K) at 157 GHz (see Appendix B for details), whereas the bias is negligible for other channels (Fig. 6).

Moreover, Fig. 1a also reveals the dynamic range and penetration depth of the four MHS channels in measuring cloud ice. Ch#2 penetrates deepest into clouds. Benefited from its low frequency (89 GHz) at which cloud scattering and water vapor absorption is lowest among the MHS channels, it produces the longest cloud PDF tail (black line in Fig. 1a). On the other end, CH#3 has the most absorption from water vapor, showing the smallest T_{cir} dynamic range. It has a slightly broader distribution on the positive half of T_{cir} PDF, compared to those of CH#4 and #5, indicating that either the upper-tropospheric water vapor from MERRA or the CRTM calculation at CH#3 contains greater uncertainty.

The CRTM is also used here to study the observed T_{cir}–IWP relationship because it can calculate cloud scattering effects if a cloud layer is specified. There are some limitations for a cloudy-sky calculation. First, the v2.0.5 CRTM assumes a fixed-width for the Gamma particle size distribution. Secondly, the number of vertical levels can not exceed 200, which might be too coarse to resolve the scattering process for thin clouds. Thirdly, the look-up-table for cloud properties in CRTM is designed only for optically thin/medium thick clouds. Hence, extrapolation induced uncertainty becomes large when we use CRTM to deal with convective/precipitating clouds. The other RTM used for studying the T_{cir}–IWP relationship is the multi-stream Cloudy-sky Radiance Model (CRM) used by the Microwave Limb Sounder (MLS) team under the spherical geometry (Wu and Jiang, 2004). It assumes spherically-homogeneous layers for atmospheric gases and clouds, with the retrieved cloud ice agreeing with CloudSat IWC within a factor of 2–4 in the upper-troposphere (Wu et al., 2009). This model allows the user to select several different particle size distributions for the Mie calculation (including the Gamma distribution) with the width a function of height. It produces a multiple scattering solution to the radiances in a cloudy atmosphere through the iterative approach. We will compare the simulation results from the CRTM and CRM with the observed T_{cir}–IWP relationship in Sect. 4.4 to explore model deficiencies at high-frequency microwave channels.

2.2 Collocated and coincident MHS-CloudSat measurements

Collocated and coincident measurements (collocations hereafter for briefness) are the incidences where two or more sensors observe the same location at the same time. These measurements provide useful pairs for instrument calibration (e.g., John et al., 2012), cross-validation of a particular variable (e.g., Wang et al., 2010), or development of new retrieval methods (e.g., Lamquin et al., 2008). In this paper, we will be focusing on the last application.

The requirements for collocated-coincident measurements may vary, depending on variability of the specific variable. Since most of the atmospheric state variables (e.g., wind, temperature, humidity) change relatively slowly and continuously with space and time compared to fast processes like clouds, their requirements for collocation and coincidence should be a bit more relaxed and the allowed windows for space and time should be consistent. In other words, the uncertainty of collocation due to spatial variations should be comparable to one of coincidence due to temporal variations. Another factor in defining the requirements for collocation and coincidence is to assure enough number of samples for statistics. For the A-train sensors, sample size is usually not a problem. For example, CloudSat footprints follow Aqua Atmospheric Infrared Sounder (AIRS) FOVs by ∼ 1 min (Kahn et al., 2008) difference. On the other hand, such a near-perfect collocation is rare between radiosonde and Global Positioning System (GPS) measurements (Sun et al., 2010). It neither occurs frequently for two satellites that run on different orbits. Adjustment of the collocating criteria becomes necessary and important in these situations.

In this study we use NOAA-18 measurements to find collocated-coincident cases with CloudSat because NOAA-18 has the closest LST to CloudSat orbit among all operational satellites with the MHS/AMSU-B instruments (Holl et al., 2010). The requirements for collocation and coincidence are 10 km in space and 15 min in time, which yield a total of 6×10^5 samples in the tropics (25° S and 25° N) during June 2006–March 2011. Holl et al. (2010) obtained an order of magnitude more collocated NOAA18-CloudSat measurements with a requirement of the same time difference but 15 km in distance, of which the number increase is roughly proportional to the area differences between the two distance criteria. The sensitivity of retrieval algorithm to the choice of collocation criteria will be discussed in the next section.

Because of the close orbits between NOAA-18 and CloudSat, the number of collocated measurements peaks at the MHS nadir angle and drops off similarly at the left and right view angles (Fig. 2). There is no significant scan angle-dependent sampling biases, which would be a factor to consider in the derived T_{cir}–IWP relationship. The number of collocation decreases sharply at oblique views with scan angle $\theta > 35°$, which may affect the statistical significance of the derived T_{cir}–IWP relationship.

In the case of highly inhomogeneous clouds, larger uncertainty is expected for the IWP within MHS FOV, as CloudSat footprints cover at most 6.7 % of the area of a MHS footprint. As a matter of fact, multiple CloudSat cloud profiles often correspond to an MHS footprint because the CloudSat footprint ($\sim$ 1.5 km) is much smaller than the spatial range of the defined collocation. Thus, we average all the CloudSat IWP values within the collocated MHS FOV to represent the mean IWP for the MHS footprint. Same procedure is applied to calculate the mean cloud top height (h_{t}) at that MHS footprint, where each individual CloudSat h_{t} is obtained by searching for the highest level where $\mathrm{IWC} > 10\,\mathrm{g\,m^{-3}}$.

3 Empirical T_{cir} model and IWP retrieval

3.1 Empirical T_{cir}–IWP relationships

For nadir-viewing sensors like MHS/AMSU-B, negative T_{cir} is caused primarily by ice cloud scattering instead of by emission. The Mie theory shows that T_{cir} is proportional to cloud IWP at microwave wavelengths and to the fourth power of frequency. As the ice cloud becomes radiatively thick, cloud self-extinction prevents T_{cir} from penetrating deeper to sense the entire IWP but rather, it has a sensitivity to pIWP. Hence, an empirical T_{cir}–IWP relationship is derived in the following format:

$$T_{\mathrm{cir}} = T_{\mathrm{cir0}} \cdot \left(1 - e^{-\mathrm{IWP}/_{H}}\right) \tag{2}$$

where T_{cir0} is the coldest T_{cir} (i.e., saturation value) and H is the parameter to determine where T_{cir} becomes saturated. Both T_{cir0} and H depend on frequency and can vary with cloud top height (h_{t}), instrument view angle, temperature lapse rate (γ) in the upper troposphere. In this study, since we focus on the tropical region where the lapse rate variation is small, these parameters are assumed only a function of channel frequency and cloud top height. For small IWP values, $T_{\mathrm{cir}} \simeq T_{\mathrm{cir0}}(-\mathrm{IWP}/_{H})$, a linear relationship as described by Wu and Jiang (2004) for Aura MLS. As also suggested by Wu and Jiang (2004), H could be a function of cloud profile shape and ice-to-water mixing ratio inside cloud, but these dependencies have secondary effects on the T_{cir}–IWP relationship.

To derive the empirical T_{cir}–IWP relationship, we first sort all collocated measurements, CloudSat IWP (averaged onto MHS footprints) and MHS T_{cir} at near-nadir views (scan angle $\in [-5^{\circ}, 5^{\circ}]$) to generate a joint PDF separately for each MHS channel. As showed in Fig. 3, the T_{cir}–IWP relationships are scattered with the PDF peaks in good agreement with Eq. (2). We then fit the 2-D PDF to obtain T_{cir0} and H parameters in Eq. (2), which is the solid curve in Fig. 3. The fitting is carried out as follows: (1) determine T_{cir0} from the coldest T_{cir}. We search all 2010 MHS nadir data and the coldest T_{cir} as T_{cir0} for each channel. (2) We then compute H in Eq. (2) with the ordinary least squares method by fitting the T_{cir} and IWP values at peak 2-D PDF (black dots in Fig. 3) using the T_{cir0} derived from step (1).

The fitted curves represent bulk characteristics of the joint PDF. Compared to a linear regression, the residual variances decreased by at least 50 %. However, the joint PDF of CH#3, show a steeper relationship for T_{cir} and IWP at colder T_{cir} values, is not represented well by Eqn.2. Moreover, T_{cir} PDF becomes flat at small IWP values ($\mathrm{IWP} < 0.5\,\mathrm{kg\,m^{-2}}$), indicating the lower limit of T_{cir} sensitivity to IWP. The spread of 2-D

PDF reflects both natural variability and collocation error of the T_cir–IWP relationship. One of the cloud variabilities that affect the T_cir–IWP relationship is the cloud top height (h_t).

To examine the dependency of H on h_t, we further sort the collocated measurements into three height groups using the mean h_t computed from CloudSat cloud profiles: $9.5 < h_\mathrm{t} < 10.5$ km, $11.5 < h_\mathrm{t} < 12.5$ km and $13.5 < h_\mathrm{t} < 14.5$ km, each group separated by 1 km to avoid overlapping of the regression lines. These three height groups account for about 48 % of all near-nadir collocated measurements. We then apply the same fitting procedure to obtain T_cir0 and H for each height group as in Eq. (2) (solid thick lines in Fig. 4). For the three height groups, a cloud bottom height (h_b) is calculated to be within 7.5 ± 1.6 km, 8.5 ± 2.5 km and 7.4 ± 2.5 km, respectively, so that the collection represents tall and thick deep convective clouds in the tropics. The measurements with h_t below 8.5 km and above 15.5 km are too few to obtain a statistically robust T_cir–IWP relationship.

Figure 4 shows that T_cir is more sensitive to IWP for clouds with higher h_t, except for CH#3 where the situation is reversed. This variation in T_cir sensitivity is expected, according to the sensitivity expression from a conceptual cloud scattering model (Eq. 6.3 in Wu and Jiang, 2004),

$$\frac{T_\mathrm{cir}}{\tau_\mathrm{ceff}} \approx T_\mathrm{scat} - T_\mathrm{AB} \tag{3}$$

where, τ_ceff is the cloud effective optical depth that is positively correlated with IWP, T_scat is the cloud scattering radiance from a convolution of the upwelling and downwelling radiation, and T_AB is the background clear-sky radiance behind the cloud. For a given channel, T_AB is the same. For thick, high h_t clouds, T_scat is colder due to more contributions from higher altitudes, resulting a larger T_cir sensitivity to IWP. The CRM used by Wu and Jiang (2004) for Aura MLS predicts a similar but weaker h_t dependence, due to the fact that MLS is a limb sounder that observes the cloud side in its LOS rather than the cloud top seen from a nadir sensor.

Since we do not have an accurate model of H dependence on h_t, a quadratic function is assumed to interpolate and extrapolate $H(h_t)$ to the cases beyond the values at the observed h_t, i.e., $h_t = 10$, 12 and 14 km. The coefficients in Eq. (4) are solved from the observed H values for three h_t groups with the mean values at 10, 12 and 14 km. Including T_{cir0}, all the parameters of the empirically-derived T_{cir}–IWP relationships for CH#2, 4 and 5 are listed in the Look-Up-Table 1.

$$H = c_0 + c_1 h_t + c_2 h_t^2 \tag{4}$$

The h_t-dependent H parameter allows a simultaneous retrieval of h_t and IWP. By including or constraining h_t in the retrieval, it improves the IWP retrieval. Other approaches, e.g., using IR channels from the CO_2 slicing method (Kahn et al., 2008) may be used in the future to constrain h_t in the IWP retrieval. As seen in Fig. 4, the error bar for each of the three cloud groups is smaller than one without the height separation. Relaxing the collocation requirements would increase the number of measurements for statistics, but we find that it does not reduce the error bar of the derived T_{cir}–IWP relationship.

To complete the empirical model for T_{cir}–IWP relationship, we need to extend the parameters listed in Table 1 from the near-nadir case to all MHS scan angles. For off-nadir views, to account for longer off-nadir LOS (ζ is the local zenith angle), the $T_{\mathrm{cir}_{\text{off-nadir}}}$ needs to be multiplied by $\cos\zeta$ to achieve an equivalent nadir T_{cir}, assuming plane parallel cloud layers. This is not a bad assumption in the case where clouds are not opaque. For opaque clouds, inhomogeneity plays a more important role in relating off-nadir and nadir views. In other words, the scan-angle correction for T_{cir} is a function of T_{cir} as well. Thus, we develop an empirical solution for this correction, which is given in the Appendix A.

3.2 Joint retrieval of IWP and h_t

The IWP and h_t are retrieved using the sequential estimation approach as described in Rodgers (2000) and Livesey et al. (2006). Equation (5) in Livesey et al. (2006) is quoted as Eq. (5) below:

$$\mathbf{x}^{(q+1)} = \mathbf{x}^{(q)} + \mathbf{S}_x \left[\mathbf{K}^T \mathbf{S}_y^{-1} \left(\mathbf{y} - \mathbf{T}_\mathrm{cir}^{(q)}\right) + \mathbf{S}_\mathrm{a}^{-1} \left(\mathbf{a} - \mathbf{x}^{(q)}\right)\right]. \tag{5}$$

(q) annotates the q-th step of iteration. In our case, $\mathbf{x} = [\mathrm{IWP}, h_\mathrm{t}]$ is the retrieved result, $\mathbf{y} = [T_{\mathrm{cir}_2}, T_{\mathrm{cir}_4}, T_{\mathrm{cir}_5}]$ is the observation, and $\mathbf{T}_\mathrm{cir}^{(q)}$ can be calculated using Eq. (2) and $\mathbf{x}^{(q)}$. $\mathbf{K}$ is the Jacobian matrix, which is defined as:

$$\mathbf{K} = \begin{bmatrix} \frac{\partial T_\mathrm{cir}}{\partial \mathrm{IWP}} \\ \frac{\partial T_\mathrm{cir}}{\partial h_\mathrm{t}} \end{bmatrix} = \begin{bmatrix} \frac{T_\mathrm{cir0}}{H} \cdot e^{-\mathrm{IWP}/H} \\ -\frac{T_\mathrm{cir0} \cdot \mathrm{IWP}}{H^2} \cdot e^{-\mathrm{IWP}/H} \cdot (c_1 + 2c_2 h_\mathrm{t}) \end{bmatrix}. \tag{6}$$

Plotted in Fig. 5 are the analytical solutions of $\mathbf{K}$ using the coefficients listed in Table 1 and Eq. (6). $\partial T_\mathrm{cir}/\partial \mathrm{IWP}$ (left column of Fig. 5) monochromatically increases with IWP for all three channels without any singularity point or multiple solutions. However, $\partial T_\mathrm{cir}/\partial h_\mathrm{t}$ (right column of Fig. 5) has a singularity point at $h_\mathrm{t} = 18\,\mathrm{km}$ for CH#2, where multiple solutions exist. For CH#5, multiple solutions can also occur for h_t. If we define the bottom of $\partial T_\mathrm{cir}/\partial h_\mathrm{t}$ curve as $h_{\mathrm{t}_\mathrm{critical}}$, then the smaller the IWP is, the higher $h_{\mathrm{t}_\mathrm{critical}}$ is. For instance, $h_{\mathrm{t}_\mathrm{critical}}$ at $\mathrm{IWP} = 3.0\,\mathrm{kg\,m^{-2}}$ is 18 km, meaning that if the cloud has an $h_\mathrm{t} > 18\,\mathrm{km}$ and $\mathrm{IWP} = 3.0\,\mathrm{kg\,m^{-2}}$, the retrieved h_t has a possibility to be underestimated. The $\mathbf{K}$ matrix response at CH#2 and CH#5 suggests that the h_t retrieval could significantly underestimate the truth when cloud top is above 18 km, especially for thick, dense clouds.

$a = [\mathrm{IWP}_0, h_{\mathrm{t}_0}]$ is the apriori (initial guess) of x. In practice, if T_cir from all three channels are less than $-5\,\mathrm{K}$, there is a strong possibility of ice cloud presence, and h_{t_0} is set to 5 km to speed up the convergence of the iteration. Otherwise, h_{t_0} is set to 0 km

Title Page
Abstract | Introduction
Conclusions | References
Tables | Figures
|◀ | ▶|
◀ | ▶
Back | Close
Full Screen / Esc
Printer-friendly Version
Interactive Discussion

instead. The initial guess of IWP_0 is always set to 0. Once the iteration begins, a is forced to equal to $x^{(q)}$ to avoid “artificial preference” of retrievals to the apriori. That is to say, the last term on the right-hand-side of Eq. (5) can be eliminated. The total number of iteration step is set to 20 regardless the final results converge or not. Within each iteration, $\mathrm{IWP}^{(q)}$ is not allowed to exceed $25\,\mathrm{kg\,m^{-2}}$ or become negative, and $h_\mathrm{t}^{(q)}$ value must be within the range of [0, 18 km]. The lower bounds assure physically meaningful solutions. The upper bound of h_t is where CH#2 and CH#5 are problematic to retrieve a trustable h_t with the set of coefficients listed in Table 1. Therefore, the protection of h_t solution again significantly under-evaluates the h_t for those high, dense clouds. Nevertheless, IWP rarely exceeds $25\,\mathrm{kg\,m^{-2}}$, and the monochromaticity of $\mathbf{K}$ with respect to IWP assures the robustness of IWP retrievals.

$\mathbf{S}_y$, $\mathbf{S}_\mathrm{a}$ and $\mathbf{S}_x$ are the matrices describing the error covariances associated with the measurements, the apriori, and the final retrieval results, respectively. $\mathbf{S}_y = [5, 5, 5]^2\,\mathrm{K}^2$ as the measurement error is estimated to be 5 K (Sect. 2.1.3). $\mathbf{S}_\mathrm{a}$ defines the step allowed to jump in each iteration, which needs to be small in very nonlinear cases where multiple solutions exist and large steps could result in an unstable retrieval. Since the retrieval function is monotonic for all channels, a large step $\mathbf{S}_\mathrm{a} = [6\,\mathrm{kg\,m^2}, 6\,\mathrm{km}]^2$ is chosen, as in the so-called Newtonian iteration, to accelerate the retrieval convergence. Once $\mathbf{S}_y$ and $\mathbf{S}_\mathrm{a}$ are fixed, $\mathbf{S}_x$ at each iteration step can then be calculated through Eq. (7):

$$\mathbf{S}_x = \left[\mathbf{K}^T \mathbf{S}_y^{-1} \mathbf{K} + \mathbf{S}_\mathrm{a}^{-1}\right]^{-1}. \tag{7}$$

The retrieval is not carried out if T_cir at all three channels are greater than 5 K, a strong indication of clear-sky. In that case, we directly assign a clear-sky flag to the scene. CH#2 radiance is excluded for retrievals over arid areas because of its contamination by surface signals. This is realized by checking land pixels with $T_\mathrm{cir} < -5\,\mathrm{K}$ for all three channels (i.e., ice cloud likely). As long as this criterion is not satisfied, only CH#4 and 5 are used for the retrieval over land, whereas CH#2 is always used over oceans. After retrieval, IWP value that has the standard deviation ($\sqrt{\mathbf{S}_x[1]}$) greater than or equal to itself is flagged as "bad quality", so does h_t. The rests are flagged as good quality.

4 Assessment of IWP and h_t retrievals

Comparisons of IWP retrievals have been challenging and sometimes even confusing because not all sensors measure the same portion of pIWP. Different cloud bottom and top heights can affect the cloud ice sensitivity and retrieval results. For MHS, the channel penetration depth varies with water vapor loading above cloud and with liquid water amount inside cloud if it is a mixed-phase case. In addition, cloud inhomogeneity along LOS introduces more uncertainties to this comparison task. Active microwave sensors such as CloudSat do not have the penetration depth issue for most clouds. In this study we treat its IWP as the truth when comparing with the measurements from passive sensors (e.g., Wu et al., 2009). Since the retrieval algorithm developed here is constrained by CloudSat IWP, the IWP retrieved from MHS is expected to be statistically close to CloudSat cloud ice. In this section we compare the PDFs of monthly IWP as well as the mean IWP maps for MHS and CloudSat data.

4.1 Comparison of IWP PDFs

Normalized PDF has been used to compare the cloud ice products and sensitivities from multiple sensors (Su et al., 2009; Wu et al., 2009). The fundamental assumption of this approach is that cloud ice should have the same probability distribution if both sensors are measuring the same ensemble of clouds (e.g., in similar latitude region and local time hour). Therefore, if the MHS PDF is smaller (greater) than that from CloudSat, we consider the retrieval is under- (over-) estimated.

Unlike the apple-to-apple comparison, vast data can be digested in one PDF plot that reveals ample information. The basic philosophy of this approach is that the variable of interest should have the same probability of observing a certain value with what the nature shows within the product's visibility range. Therefore, if the probability is smaller (greater) than that from the truth, the variable (e.g., cloud occurring frequency) is under- (over-) estimated.

As expected for the CloudSat-constrained retrieval, MHS IWP PDF agrees well with CloudSat, as shown by the grey and black lines in Fig. 6. The decreasing probability with IWP reflects natural variability of cloud ice. CloudSat IWPs here are 15-FOV averaged values in order to match the MHS footprint size, which is slightly steeper than the original (non-averaged) PDF, or higher (lower) possibility at smaller (larger) IWP. The averaging effect ($< 10\,\%$) is negligible compared to the differences among various datasets/retrievals. When all good and bad retrievals from the 90 MHS views are included, the PDF (solid black line) in Fig. 6 rises more sharply at small IWPs ($\sim 500\,\mathrm{g\,m^{-2}}$) due to the arbitrary retrieval suppression for negative IWP values and false detection of clear-sky scenes. The dropping PDF at IWP $< 500\,\mathrm{g\,m^{-2}}$ is mostly noise. When the quality flag is applied to exclude bad retrievals, the PDF (dots) agrees better with CloudSat at IWP $> 300\,\mathrm{g\,m^{-2}}$. At large values ($> 8 \times 10^3\,\mathrm{g\,m^{-2}}$), our algorithm tends to slightly over-estimate IWP when compared to CloudSat.

The PDF of NOAA operational MSPPS data (crosses in Fig. 6) is lower than CloudSat at all IWP values. At large IWP values (IWP $> 10^3\,\mathrm{g\,m^{-2}}$), it differs by 10 times or more, indicating that the operational product significantly underestimate cloud ice, compared to CloudSat. This low bias was also reported in other studies (e.g., Waliser et al., 2009; Eliasson et al., 2011).

The quality of our cloud ice retrieval is demonstrated clearly in a scene over Hurricane Earl on 31 August 2010 (Fig. 7a–c). T_{cir} in all three MHS channels captured the structure of Hurricane Earl very well, showing the eye, eye wall and spiral rain bands. CH#2 radiances, penetrating the deepest, reveal more ice cloud structures than other channels. The retrieved IWP from our algorithm (Fig. 7d) retains most of the fine structures in CH#2 and also shows a hint of additional two outer arms. Although the values of these arms are below the noise level, they are probably real because they are also present in geostationary satellite IR image (not shown). The IWPs from CloudSat overpass (colored crosses) have slightly larger values than MHS, whereas MSPPS operational IWP (Fig. 7f) are significantly smaller than CloudSat and our retrievals. This hurricane case also highlights the value of MHS IWP in studying the 2-D atmospheric dynamics and cloud structures that are not captured by the CloudSat curtain sampling. Using the CloudSat-constrained IWP measurements, we can obtain a good spatial and temporal coverage from the MHS/AMSU-B sensors onboard all operational satellites.

Retrieved h_t (Fig. 7e) also agree reasonably well with CloudSat, especially at the hurricane periphery and the eye wall, but are lower by ~ 4 km over the hurricane deck (13 km versus > 18 km). This is probably due to the fact that the cloud top at the deck is dominantly higher than those at the hurricane periphery, i.e., higher than 18 km. They hence exceed the upper-limit of the reliable h_t retrieval range from our algorithm. Pixel-by-pixel comparisons are done for some other cases that have CloudSat cloud tops lower than 18 km, and the h_t retrieval seems quite promising (not shown). Nevertheless, the h_t retrieval here is mainly to improve IWP retrieval, rather than the purpose of scientific study.

As the first CloudSat-calibrated column-wise IWP measurement that has an excellent spatial coverage, the MHS IWP retains numerous potential usages for model input, for validation of other instrument measurements and for model-observation comparisons in the future.

4.2 Geographic distribution of IWP

Monthly mean IWP maps show good correlation between MHS and CloudSat cloud ice for August 2010 (Fig. 8), where the correlation is 0.81 in the tropics. Sampling error is evident in these maps. With a relatively coarse grid box ($5^\circ \times 5^\circ$), the CloudSat monthly maps (Fig. 8a and c) are spotty due to a lack of swath coverage. This sampling is also aliased to the westward traveling fast cloud systems, leading to cloud ice spikes (e.g., Eastern Pacific) and scatters (e.g., Amazon Rainforest) on the CloudSat maps. The sampling bias is largely mitigated by the 90-FOV MHS swath, maps of which look much smoother instead (Fig. 8b and d) because it overpasses one grid box 6 times as often as CloudSat on average. If the footprint size is taken into consideration, MHS could pass every corner of each $5^\circ \times 5^\circ$ grid box in the tropics by as many as 42 times within a month, while CloudSat covers only 4 % of the area in the tropics. The major features between two datasets agree well, especially in deep convective regions where IWPs are large. The day-night differences of ice cloud thickness seen in CloudSat are also evident in the MHS maps, e.g., in the central America and central Africa.

Interestingly, in the scatter plot of MHS and CloudSat IWPs at a logarithm scale, the correlation is not along 1 : 1 line, showing a higher bias in MHS at smaller IWP values. The overall regression yields $\text{IWP}_{\text{CloudSat}} = (0.83 \pm 0.017)\,\text{IWP}_{\text{MHS}} - 14.7\,[\text{g m}^{-2}]$, shown as the blue dots in Fig. 9b. The $-14.7\,\text{g m}^{-2}$ offset partly comes from elevated topographies, e.g., the Andies, and from desert, e.g., central Australia. The bias is slightly worse during night (MHS descending orbit) than during the day (MHS ascending orbit). If CH#2 is included for the MHS IWP retrievals over land, the high bias would increase over Australia, which may suggest a warm bias in MERRA surface temperature in that region during nighttime (i.e., a cold bias of T_{cir} for CH#2). It is suggested that our retrieval algorithm has some limitations over complicated surface conditions, which will be discussed in the next section. Part of the $-14.7\,\text{g m}^{-2}$ offset is caused by the fact that MHS tends to slightly over-estimate IWP than CloudSat, especially for thick and dense clouds. Besides, CloudSat probably misses some convections due to its sampling bias, for instance, over amazon rainforest and marinetime continents. Visual comparison between MODIS ice cloud optical depth (Fig. 7 of Meyer et al., 2007) and MHS IWP shows better agreement at these regions.

4.3 Limitations of the algorithm

The forward model (T_{cir}–IWP relationships) and retrieval algorithm presented in this paper are designed for tropical regions and have difficulties in retrieving IWP over elevated topography and desert. In the cases of mixed-phase clouds or excessive water vapor abundance above cloud tops, the retrieval error for IWP might increase. The major causes for the biases over land are likely surface temperature error in the mountain and desert regions in the MERRA data, or the CRTM surface emissivity error in modelling the surface radiation. Since CH#2 radiance contains surface signals (CH#5 sees arid and snow surfaces as well), uncertainties in surface temperature and emissivity will induce T_{cir} biases. As a matter of fact, we do see a systematic warm bias of 2 K in CH#2 T_{cir} (Appendix B), which could be due to the instrument calibration error or T_{ccr} model error. Moreover, the PDF of T_{ccr} for CH#2 (Fig. 1b) extends to a temperature as low as 220 K, which is a strong evidence of contamination from clouds or cold surfaces (i.e., ice pack on mountains can also cause this low TB). With the development of neural network approach, the initial guess of T_{ccr} could be used to improve the cloud ice retrieval over complicated surface conditions (Chen and Staelin, 2003).

The parameters in Table 1 assume that atmospheric temperature lapse rate γ is constant in the tropics. As predicted by Wu and Jiang (2004) using CRM, the T_{cir}–IWP relationship is also a function of γ (Fig. 6.10 therein). Evaluating the PDFs of retrieved IWP outside the tropics, we find that the PDF of extratropical IWP starts to oscillate at its large-value tail (Fig. 9a) than that in the tropics (Fig. 6). The quality-controlled PDF in this case is still comparable with CloudSat PDF though for this bin assuming 100 % tolerance level of the PDF difference. Hence, our algorithm is expected to perform well within latitudes of 30° N, S, but degrades in the extratropics. The mean vertical temperature profiles are also similar to those in the tropics up to 30° in latitude (Fig. 6.9 in Wu and Jiang, 2004). At mid-to-high latitudes beyond 30°, the quality-controlled PDFs are too low or even alter its shape, and the retrieved MHS IWP merely correlate with CloudSat IWP (not shown). In the future algorithm development, γ should be treated as an independent variable, such that the algorithm can be applied for IWP retrievals at higher latitudes.

Liquid clouds occur frequently below 5 km where temperature is usually greater than 0 K (Riedi et al., 2001), which may have little impact on CH#4 but can significantly affect CH#2 and CH#5 T_{cir}. For deep convective clouds, liquid droplets can be lifted to a much higher altitude. The mixing of liquid droplets into ice cloud enhances the cloud emission contribution at microwave frequencies and hence decreases the T_{cir} sensitivity to IWP.

Wu and Jiang (2004) showed that this impact could be as large as 30–50 % in a strong mixed-phase case, which alter the relationship in Eq. (2) with different parameters. Therefore, mixed-phase clouds can contribute significantly to the spread of the 2-D PDF shown in Figs. 3 and 4.

Water vapor above and inside cloud plays a screening role in reducing the sensitivity to IWP, in a way similar to liquid droplets. Since CH#4 and 5 are water vapor channels, they are sensitive to the water vapor abundance above and inside ice clouds. As a result, T_{ccr} calculation could be biased if MERRA water vapor is too dry or too wet above clouds. The water vapor impact was only evaluated using CRM with different water vapor profiles, assuming variability within uncertainty of observed upper-troposphere water vapor. The water vapor impact is found small and negligible in these CRM simulations (less than 5 % with doubling water vapor amount above clouds).

4.4 Comparison with RTM simulations

In this section, CRTM and CRM are employed to evaluate the current model performance on simulating the observed T_{cir}–IWP relationship, and are compared with the empirical model as described in Eq. (2). The motivation of this exercise is to quantify model uncertainties and determine how reliable these RTMs are for calculating cloudy-sky radiances as observed satellite microwave channels/instruments. We would also like to identify possible causes of these model errors and develop a plan for future model improvement.

In both models, three ice clouds are fed in one-by-one with cloud bottoms at 7.5 km and cloud tops at 10, 12 and 14 km, respectively. Two cloud shapes (convection with anvil cloud top; Gaussian shape) are tested. Since their results differ little, the first cloud shape is applied to all following studies. US standard atmosphere in the tropics is used as the background atmosphere. CRM has 640 layers extending from the surface to 80 km, and the vertical resolution is ~ 150 m. For CRTM, to keep a high vertical resolution of cloud, the first 180 layers of CRM inputs are used, and the atmosphere profile tops at ~ 22 km. For the cloud droplet size distribution, CRM has several options.

Only McFarquhar–Heymsfield (MH) and Gamma distributions are tested with different combinations of parameter values. MH distribution was applied to deliver MLS IWC product (Wu et al., 2009), and Gamma size distribution was assumed for CloudSat ice water product retrievals (Austin et al., 2009). In CRTM, only the cloud ice effective radius is tunable with fixed-width Gamma size distribution assumption. Both models and the observation are compared at nadir-view only.

Comparing T_{cir} responses from different channels to the same cloud is a straightforward yet very effective way of presenting many of the differences. As one can see from Fig. 10a, T_{cir} of CH#2 is generally colder than that of CH#5 for small values, and they are nearly 1 : 1 correlated for large T_{cir} depressions (black dots). These features imply that CH#2 should have larger response to thin and medium thick clouds, and the penetration depths of the two channels are about the same when encounter dense and thick clouds. Raw T_{B} from the two channels showed the same features (not shown). CRTM produces almost identical reposes for CH#2 and CH#5, both of which are however too weak compared with the observation (triangles). CRM produces comparable dynamical ranges of T_{cir} with effective radius of 160 µm and width parameter of 2 (refer to Evans et al., 1998 for the format of Gamma distribution), but it always generates a weaker response for CH#2, contradicting with the observation (crosses), while the T_{cir}–IWP relationship for CH#5 is simulated quite well. The main caveat of CRM is that it only considers scattering while ignores the ice emission. If cloud induced radiation is dominated by emission, the volume extinction coefficient is approximately proportional to channel frequency, i.e., ice emission is more important for CH#5 than CH#2. Since ice emission contribution to T_{cir} is opposite to that from cloud scattering, a shallower T_{cir} response for CH#5 is expected to occur. The observed CH#2/CH#5 T_{cir} ratio suggests that ice cloud emission offsets as much as 30 % of cloud scattering impact for thin and medium thick clouds, while cloud scattering dominates for dense and thick clouds. Moreover, liquid droplets in mixed-phase clouds could contribute more to the emissions and further reduce the CH#5 T_{cir} response. That may explain the difference between CRTM and the observation.

The models simulate the observed T_{cir} ratio between CH#4 and 5 better, as shown in Fig. 10b. Nevertheless, models tend to over-predict the CH#4 response. Because CH#4 is closer to the 183.3 GHz water vapor absorption line, it is more sensitive to water vapor variations than CH#5. Therefore, the air above cloud top might have been drier than the ambient air to lead to a smaller magnitude of CH#4 T_{cir}. This derivation is supported by some observational evidences for deep convective clouds (e.g., Chae et al., 2011). Again, CRTM overall produces weaker T_{cir}, probably due to the heavy extrapolation from thin cloud LUT to thicker clouds, and the narrow fixed-width Gamma size distribution.

To summarize, RTMs are not as good as the empirical models in capturing the observed T_{cir}–IWP relationships for tropical ice cloud. Some plausible explanations are given to explain the observed model discrepancies, which include but not limited to the overlook of emission from liquid droplets and ice particles, indifference of humidity above clouds and ambient air, and too narrow width of Gamma size distribution. One should be adviced that Gamma distribution is not indicated as the best cloud ice particle size distribution. Rather, it reflects the inter-model consistency between the two RTMs and the original assumptions made for CloudSat IWP retrievals. Since CRTM serves as the center piece of NOAA and NASA data assimilation systems, and CRM is used for MLS cloud property retrievals, this part of work is of much interest to a broad community.

5 Conclusions

A fast empirical forward model built upon T_{cir}–IWP relationships at MHS 157, 183.3 ± 3 and 190.3 GHz channels is developed and used to retrieve tropical cloud IWP from MHS radiance measurements. The T_{cir}–IWP relationship at these channels are dependent on cloud top height h_{t} in the tropics (Fig. 4), and the algorithm for retrieving IWP and h_{t} simultaneously can improve the IWP accuracy. The IWP PDFs from MHS and CloudSat retrievals agree quite well, as expected for this constrained empirical forward model, over a wide dynamic range of cloud ice (IWP = 0.5 – 10 kg m^{-2}, Fig. 6). The empirical forward model is valid for clouds with h_t lower than 18 km and IWP greater than 0.5 kg m^{-2}, but only in the tropics between 30° S and 30° N at present (Fig. 9). Beyond that latitude range, temperature lapse rate variations need to be taken into account to refine the T_{cir}–IWP relationship. In addition, the algorithm still has some issues in retrieving IWP over elevated and arid topography (Fig. 8).

Producing a CloudSat-consistent MHS IWP product has several direct benefits and important implications for studying clouds. Firstly, it helps to extend CloudSat cloud coverage with a wider swath width because frequent sampling from different operational satellites will allow frequent updates of fast-evolving weather phenomena such as hurricane and frontal system. The new data can be used to improve weather prediction (e.g., cloud diurnal cycle) and long-term regional climate monitoring (e.g., IWP trend). Secondly, our improved IWP retrieval method renders generally larger IWP values than the NOAA operational product (Figs. 6 and 7). The approach we implemented with high-frequency microwave channels improves cloud detection in scenes with low IWP. Comparing with CloudSat monthly climatology as well as the single-orbit measurements, we found that our results are closer to CloudSat integrated ice water path. Thirdly, we show that substituting 89 GHz channel with 183.3 GHz channels for cloud ice retrieval reduces false detection of ice clouds and improves sensitivity to IWP as the higher-frequency channels are more sensitive to ice particle scattering. Lastly, the derived empirical T_{cir}–IWP relationships can be used to evaluate RTM simulations of cloudy-sky radiances, validate model assumptions, and improve model skills for data assimilation applications in the future (Fig. 10).

Although the empirical T_{cir}–IWP relationship developed here was from NOAA-18 MHS, it is applicable to the similar channels used by other AMSU-B/MHS instruments on NOAA and Metop operational satellites for obtaining a longer data record and more frequent coverage. It can also be applied to other instruments that have the same combination of channels, for example, Advanced Technology Microwave Sounder (ATMS) onboard Suomi-NPP satellite, Special Sensor Microwave Imager/Sounder

(SSMI/S) onboard the Air Force F-16, F-17 and F-18 satellites. Furthermore, the approach we demonstrated in this study can be applied to IR/VIS sensors with the measurements collocated with CloudSat, such as Aqua Atmospheric Infrared Sounder (AIRS) and MODIS, to extend the sensitivity to lower IWP values and enhance the dynamic range of remote sensing of cloud ice from space.

Appendix A

Converting off-nadir T_{cir} to nadir T_{cir}

The collocation occurrences near outmost views are too few to make a statistically meaningful T_{cir}–IWP relationship, as shown in Fig. 2. An alternative way is to seek a conversion factor such that the PDF of converted off-nadir T_{cir} matches that of the nadir T_{cir}, in which case the nadir T_{cir}–IWP relationship can then be applied.

If the cloud layer can be assumed plane-parallel and is not completely opaque to MHS, $\mathrm{PDF}_{\mathrm{side}} \cdot \cos\zeta = \mathrm{PDF}_{\mathrm{nadir}}$ roughly holds (thick solid lines in Fig. A1a), where ζ is the solar zenith angle. This relationship means that, with equal probability of seeing a cloud, the off-nadir cloud T_{cir} is colder than that from the nadir-view, mainly due to the longer integration length of cloud water path. However, such a relationship begins to lose its validity as the ice clouds become opaque at oblique views. As shown in Fig. A1b, the PDF curves become much more flat at $T_{\mathrm{cir}} = -100\,\mathrm{K}$ compared with those at $T_{\mathrm{cir}} = -50\,\mathrm{K}$. A factor of $\cos(\zeta/2.1)$ can roughly capture such a view-dependency. In the most extreme case, where T_{cir} saturates at all view angles, the PDFs should become independent on the view-angle, where the factor can be set as $\cos(\zeta/\infty)$.

By defining $F = \cos(\zeta/\mathrm{fac})$, we can convert the off-nadir T_{cir} to the equivalent nadir T_{cir} by multiplying the former by F, i.e.,

$$T_{\mathrm{cir}}\big|_{\mathrm{side}} \cdot F = T_{\mathrm{cir}}\big|_{\mathrm{equivalent\ nadir}}. \quad \text{(A1)}$$

fac = $f(T_{\mathrm{cir}}, \mathrm{CH\#})$ is a function of T_{cir} and the choice of channel number, which is estimated from the observation to follow such relationships:

$$\mathrm{fac(CH\#2)} = \begin{cases} 0.7764 \cdot e^{-0.0077 T_{\mathrm{cir}}} & \text{if } T_{\mathrm{cir}} > -120\,\mathrm{K} \\ 1 & \text{if } 0.7764 \cdot e^{-0.0077 T_{\mathrm{cir}}} < 1 \\ 100 & \text{if } T_{\mathrm{cir}} \leq -120\,\mathrm{K} \end{cases} \quad \text{(A2)}$$

$$\mathrm{fac(CH\#4)} = \begin{cases} 0.0013 \cdot e^{-0.1034 T_{\mathrm{cir}}} & \text{if } T_{\mathrm{cir}} > -120\,\mathrm{K} \\ 1 & \text{if } 0.0013 \cdot e^{-0.1034 T_{\mathrm{cir}}} < 1 \\ 100 & \text{if } T_{\mathrm{cir}} \leq -80\,\mathrm{K} \end{cases} \quad \text{(A3)}$$

$$\mathrm{fac(CH\#5)} = \begin{cases} 0.8160 \cdot e^{-0.0098 T_{\mathrm{cir}}} & \text{if } T_{\mathrm{cir}} > -120\,\mathrm{K} \\ 1 & \text{if } 0.8160 \cdot e^{-0.0098 T_{\mathrm{cir}}} < 1\,. \\ 100 & \text{if } T_{\mathrm{cir}} \leq -120\,\mathrm{K} \end{cases} \quad \text{(A4)}$$

Appendix B

Correction of T_{cir} for CH#2

As shown by the black line in Fig. 1a, the PDF peak for T_{cir} of CH#2 is at 2 K instead of 0 K at the nadir view. Further examination of other months of T_{cir} PDFs for this channel shows the same warm bias (named as ΔT). At off-nadir views, ΔT becomes smaller, which follows the theoretical clear-sky limb-darkening curve $\Delta T_{\mathrm{nadir}} \cdot \cos\zeta = \Delta T_{\mathrm{side}}$. That means the estimated T_{ccr} for clear-sky has a systematic error at 157 GHz, which could originate from the inaccuracy of MERRA atmosphere profiles or corrigendum inside CRTM. To account for this offset, all T_{cir} for CH#2 is subtracted by this offset before carrying out the retrieval:

$$T_{\mathrm{cir}}(\mathrm{CH\#2}) = T_{\mathrm{cir}}(\mathrm{CH\#2})_{\mathrm{calculated}} - 2 \cdot \cos\zeta. \quad \text{(B1)}$$

Acknowledgements. This work is performed at NASA Goddard Space Flight Center with support from NASA NNH10ZDA001N-ESDRERR (Earth System Data Records Uncertainty Analysis) project. The authors are grateful to S. Buehler, V. John, I. Moradi, S. Wong for helpful discussions and comments. We thank the two anonymous referees for their reviews. AAPP is provided by EUMETSAT network of satellite application facilities. Copyright 2013. All rights reserved.

References

Arriaga, A.: Technical memorandum No. 5: Microwave Humidity Sounder (MHS) simulations with a radiative transfer model, EUMETSAT technical report, EUMESAT, 2000. 8193

Atkinson, N. C.: Calibration, monitoring and validation of AMSU-B, Adv. Space. Res., 28, 117–126, 2001. 8194

Austin, R. T., Heymsfield, A. J., and Stephens, G. L.: Retrievals of ice cloud microphysical parameters using the CloudSat millimeter-wave radar and temperature, J. Geophys. Res., 114, D00A23, doi:10.1029/2008JD010049, 2009. 8189, 8195, 8212

Buehler, S. A., Kuvatov, M., and John, V. O.: Scan asymmetries in AMSU-B data, Geophys. Res. Lett., 32, L24810, doi:10.1029/2005GL024747, 2005. 8194

Chae, J. H., Wu, D. L., Read, W. G., and Sherwood, S. C.: The role of tropical deep convective clouds on temperature, water vapor, and dehydration in the tropical tropopause layer (TTL), Atmos. Chem. Phys., 11, 3811–3821, doi:10.5194/acp-11-3811-2011, 2011. 8213

Chahine, M. T.: The hydrological cycle and its influence on climate, Nature, 359, 373–380, 1992. 8188

Chen, F. W. and Staelin, D. H.: AIRS/AMSU/HSB precipitation estimates, IEEE T. Geosci. Remote, 41, 410–417, doi:10.1109/TGRS.2002.808322, 2003. 8210

Chen, W.-T., Woods, C. P., Li, J.-L. F., Waliser, D. E., Chern, J.-D., Tao, W.-K., Jiang, J.-H., and Tompkins, A. M.: Partitioning CloudSat ice water content for comparison with upper tropospheric ice in global atmospheric models, J. Geophys. Res., 116, D19206, doi:10.1029/2010JD015179, 2011. 8191

Eliasson, S., Buehler, S. A., Milz, M., Eriksson, P., and John, V. O.: Assessing observed and modelled spatial distributions of ice water path using satellite data, Atmos. Chem. Phys., 11, 375–391, doi:10.5194/acp-11-375-2011, 2011. 8189, 8191, 8194, 8195, 8207

Evans, K. F., Walter, S. J., Heymsfield, A. J., and Deeter, M. N.: Modeling of Submillimeter Passive Remote Sensing of Cirrus Clouds, J. Appl. Meteorol., 37, 184–205, 1998. 8212

Gong, J. and Wu, D. L.: View-angle-dependent AIRS cloudiness and radiance variance: Analysis and interpretation, J. Geophys. Res.-Atmos., 118, 2327–2339, doi:10.1002/jgrd.50120, 2013. 8197

Holl, G., Buehler, S. A., Rydberg, B., and Jiménez, C.: Collocating satellite-based radar and radiometer measurements – methodology and usage examples, Atmos. Meas. Tech., 3, 693–708, doi:10.5194/amt-3-693-2010, 2010. 8191, 8194, 8195, 8199, 8200

John, V. O., Holl, G., Buehler, S. A., Candy, B., Saunders, R. W., and Parker, D. E.: Understanding inter-satellite biases of microwave humidity sounders using global SNOs, J. Geophys. Res., 117, D02305, doi:10.1029/2011JD016349, 2012. 8192, 8199

John, V. O., Holl, G., Atkinson, N., and Buehler, S. A.: Monitoring scan asymmetry of microwave humidity sounding channels using simultaneous all angle collocations (SAACs), J. Geophys. Res., 118, 1536–1545, doi:10.1002/jgrd.50154, 2013. 8194

Kahn, B. H., Chahine, M. T., Stephens, G. L., Mace, G. G., Marchand, R. T., Wang, Z., Barnet, C. D., Eldering, A., Holz, R. E., Kuehn, R. E., and Vane, D. G.: Cloud type comparisons of AIRS, CloudSat, and CALIPSO cloud height and amount, Atmos. Chem. Phys., 8, 1231–1248, doi:10.5194/acp-8-1231-2008, 2008. 8199, 8203

Lamquin, N., Stubenrauch, C. J., and Pelon, J.: Upper tropospheric humidity and cirrus geometrical and optical thickness: relationships inferred from 1 year of collocated AIRS and CALIPSO data, J. Geophys. Res., 113, D00A08, doi:10.1029/2008JD010012, 2008. 8199

Li, J.-L., Li, F., Waliser, D. E., Chen, W.-T., Guan, B., Kubar, T., Stephens, G., Ma, H.-Y., Deng, M., Donner, L., Seman, C., and Horowitz, L.: An observationally based evaluation of cloud ice water in CMIP3 and CMIP5 GCMs and contemporary reanalyses using contemporary satellite data, J. Geophys. Res., 117, D16105, doi:10.1029/2012JD017640, 2012. 8188, 8189

Liu, Q. and Weng, F.: Advanced Doubling – Adding Method for Radiative Transfer in Planetary Atmospheres, J. Atmos. Sci., 63, 3459–3465, 2006. 8196

Livesey, N. J., Snyder, W. V., Read, W. G., and Wagner, P. A.: Retrieval algorithms for the EOS Microwave Limb Sounder (MLS), IEEE T. Geosci. Remote, 44, 1144–1155, 2006. 8204

Meyer, K., Yang, P., and Gao, B.-C.: Tropical ice cloud optical depth, ice water path, and frequency fields inferred from the MODIS level-3 data, Atmos. Res., 85, 171–182, 2007. 8209

McFarquhar, G. M. and Heymsfield, A. J.: Parameterization of tropical cirrus ice crystal size distributions and implications for radiative transfer: results from CEPEX, J. Atmos. Sci., 54, 2187–2200, 1997. 8189

McNally, A. P., Watts, P. D., Smith, J. A., Engelen, R., Kelly, G. A., Thepaut, J. N., and Matricardi, M.: The assimilation of AIRS radiance data at ECMWF, Q. J. Roy. Meteorol. Soc., 132, 935–957, 2006. 8197

Protat, A., Bouniol, D., Delanoe, J., O'Connor, E., May, P. T., Plana-Fattori, A., Hasson, A., Gorsdorf, U., and Heymsfield, A. J.: Assessment of Cloudsat Reflectivity Measurements and Ice Cloud Properties Using Ground-Based and Airborne Cloud Radar Observations, J. Atmos. Ocean. Tech., 26, 1717–1741, 2009. 8195

Pulliainen, J., and Hallikainen, M.: Retrieval of Regional Snow Water Equivalent from Space-Borne Passive Microwave Observations, Remote. Sens. Environ., 75, 76–85, 2001. 8191

Ramaswamy, V. and Ramanathan, V.: Solar absorption by cirrus clouds and the maintenance of the tropical upper troposphere thermal structure, J. Atmos. Sci., 46, 2293–2310, 1989. 8188

Richter, J. and Rasch, P.: Effects of convective momentum transport on the atmospheric circulation in the Community Atmosphere Model, version 3, J. Climate, 21, 1487–1499, 2008. 8188

Riedi, J., Goloub, P., and Marchand, R. T.: Comparison of POLDER cloud phase retrievals to active remote sensors measurements at the ARM SGP site, Geophys. Res. Lett., 28, 2185–2188, 2001. 8210

Rodgers, C. D.: Inverse methods for atmospheric science, theory and practice, http://www.amazon.com/Inverse-Methods-Atmospheric-Sounding-Planetary/dp/981022740X, last access: September 2013, World Scientific, 2000. 8204

Seo, E.-K. and Liu, G.: Determination of 3-D cloud ice water contents by combining multiple data sources from satellite, ground radar, and a numerical model, J. Appl. Meteorol., 45, 1494–1504, doi:10.1175/JAM2430.1, 2006. 8193

Soden, B. J.: Tracking upper tropospheric water vapor radiances: A satellite perspective, J. Geophys. Res., 103, 17069–17081, doi:10.1029/98JD01151, 1998. 8193

Stephens, G. L., Tsay, S. C., Stackhouse, P. W., and Flatau, P. J.: The relevance of the microphysical and radiative properties of cirrus clouds to climate and climatic feedback, J. Atmos. Sci., 47, 1742–1754, 1990. 8188

Strow, L. L., S. E. Hannon, S. De-Souza Machado, H. E. Motteler, and D. C. Tobin: Validation of the Atmospheric Infrared Sounder radiative transfer algorithm, J. Geophys. Res., 111, D09S06, doi:10.1029/2005JD006146, 2006.

Su, H., Jiang, J. H., Stephens, G. L., Vane, D. G., and Livesey, N. J.: Radiative effects of upper tropospheric clouds observed by Aura MLS and CloudSat, Geophys. Res. Lett., 36, L09815, doi:10.1029/2009GL037173, 2009. 8206

Sun, B., Reale, A., Seidel, D. J., and Hunt, D. C.: Comparing radiosonde and COSMIC atmospheric profile data to quantify differences among radiosonde types and the effect of imperfect collocation on comparison statistics, J. Geophys. Res., 115, D23104, doi:10.1029/2010JD014457, 2010. 8199

Waliser, D. E., Li, J.-L. F., Woods, C. P., Austin, R. T., Bacmeister, J., Chern, J., Genio, A. D., Jiang, J. H., Kuang, Z., Meng, H., Minnis, P., Platnick, S., Rossow, W. B., Stephens, G. L., Sun-Mack, S., Tao, W.-K., Tompkins, A. M., Vane, D. G., Walker, C., and Wu, D.: Cloud ice: A climate model challenge with signs and expectations of progress, J. Geophys. Res., 114, D00A21, doi:10.1029/2008JD010015, 2009. 8189, 8191, 8195, 8207

Wang, L.-K., Wu, X.-Q., Goldberg, M., Cao, C.-Y., Li, Y.-P., and Sohn, S.-H.: Comparison of AIRS and IASI radiances using GEOS imagers as transfer radiometers toward climate data record, J. Appl. Meteor. Climatol., 49, 478-492, 2010. 8199

Weng, F., Zhao, L., Ferraro, R. R., Poe, G., Li, X., and Grody, N. C.: Advanced microwave sounding unit cloud and precipitation algorithms, Radio Sci., 38, 8068, doi:10.1029/2002RS002679, 2003. 8194

Wu, D. L. and Jiang, J. H.: EOS MLS Algorithm Theoretical Basis for Cloud Measurements, Technical Report, D-19299/CL#04-2160, ATBD-MLS-06, http://mls.jpl.nasa.gov/data/eos_algorithm_atbd.pdf?, last access: September 2013, Jet Propulsion Laboratory, 2004. 8198, 8201, 8202, 8210, 8211

Wu, D. L., Read, W. G., Dessler, A. E., Sherwood, S. C., and Jiang, J. H.: UARS/MLS Cloud Ice Measurements: Implications for H_2O Transport near the Tropopause, J. Atmos. Sci., 62, 518–530, 2005. 8196

Wu, D. L., Austin, R. T., Deng, M., Durden, S. L., Heymsfield, A. J., Jiang, J. H., Lambert, A., Li, J.-L., Livesey, N. J., McFarquhar, G. M., Pittman, J. V., G. L. Stephens, S. Tanelli, D. G. Vane, and D. E. Waliser: Comparisons of global cloud ice from MLS, CloudSat, and correlative data sets, J. Geophys. Res., 114, D00A24, doi:10.1029/2008JD009946, 2009. 8189, 8190, 8191, 8194, 8195, 8196, 8198, 8206, 8212

Wu, D. L., Lambert, A., Read, W. G., Eriksson, P., and Gong, J.: MLS and CALIOP cloud ice measurements in the upper troposphere: A constraint from microwave on cloud microphysics, J. Appl. Meteorol. Clim., doi:10.1175/JAMC-D-13-041.1, in press, 2013. 8196

Zhao, L.-M. and Weng, F.-Z.: Retrieval of Ice Cloud Parameters Using the Advanced Microwave Sounding Unit, J. Appl. Meteorol., 41, 384–395, doi:10.1175/1520-0450(2002)041<0384:ROICPU>2.0.CO;2, 2002. 8190, 8194

Table 1. Look-up-table for the parameters of the joint IWP-h_t retrieval.

	T_{cir0} [K]	c_0 [kg m^{-2}]	c_1 [g m^{-3}]	c_2 [mg m^{-4}]
CH#2	−172	21.45	−1.9875	0.5625
CH#4	−140	17.021	−0.4078	0
CH#5	−155	29.6511	−2.26214	0.038156

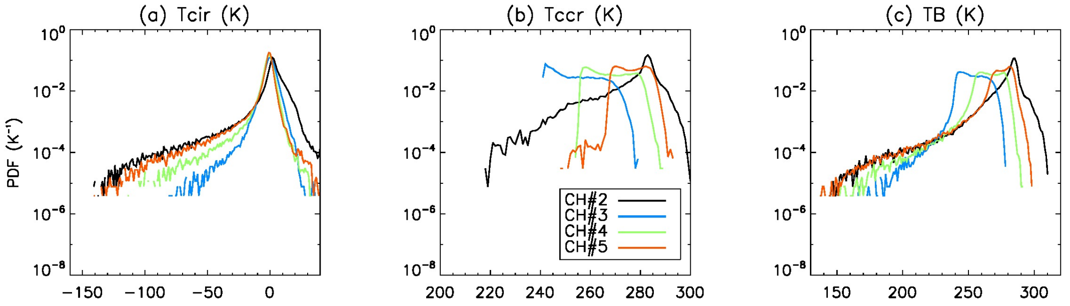

Fig. 1. Probability density functions of T_{cir} **(a)**, T_{ccr} **(b)** and T_{B} **(c)** for CH#2 (black), #3 (blue), #4 (green) and #5 (red). Samples are from NOAA-18 MHS nadir-view during August 2010 in the tropics (25° S, 25° N).

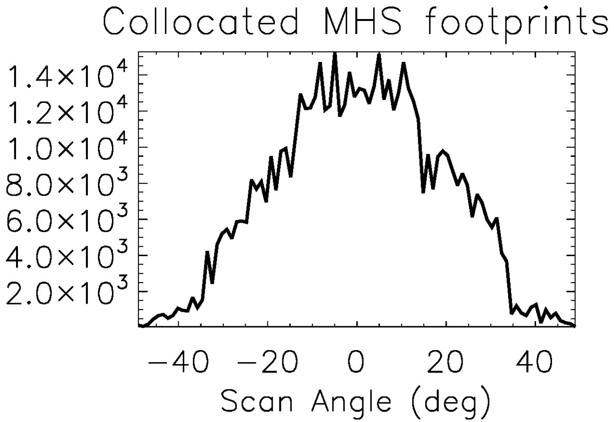

Fig. 2. Total number of collocated and coincident MHS footprints as a function of scan angle between June 2006 and March 2011.

Title Page
Abstract Introduction
Conclusions References
Tables Figures
◀I ▶I
◀ ▶
Back Close
Full Screen / Esc
Printer-friendly Version
Interactive Discussion

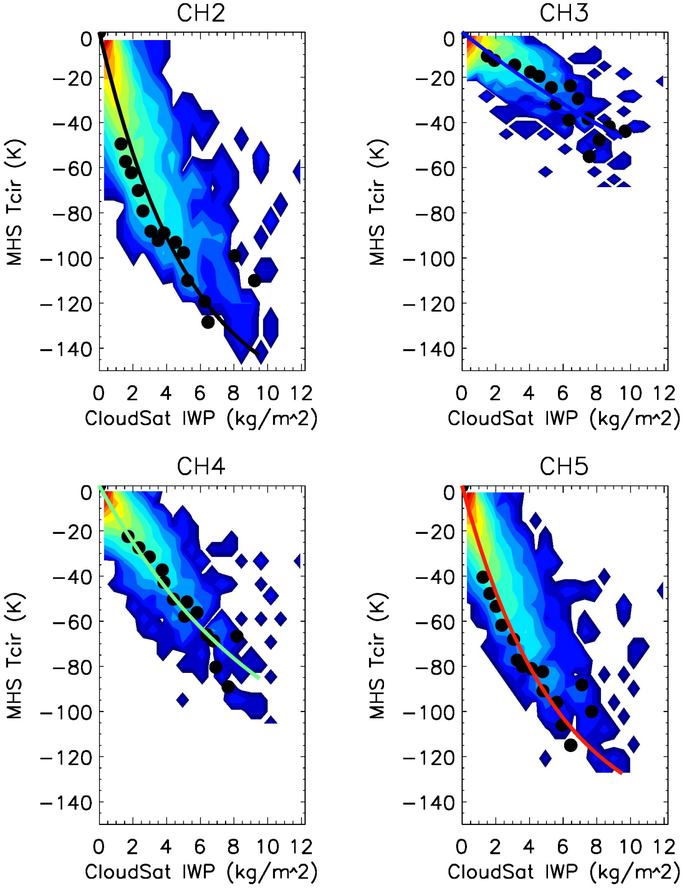

Fig. 3. Countours of 2-D PDFs (normalized by the maximum value of the histogram) of collocated CloudSat IWP (abscissa, averaged onto MHS footprints) and MHS T_{cir} (ordinate) for CH#2–CH#5 at near-nadir views (scan angle $\in [-5^\circ, 5^\circ]$). Black dots locate the peak of the 2-D PDFs, and the thick solid lines are regression curves using Eqs. (2).

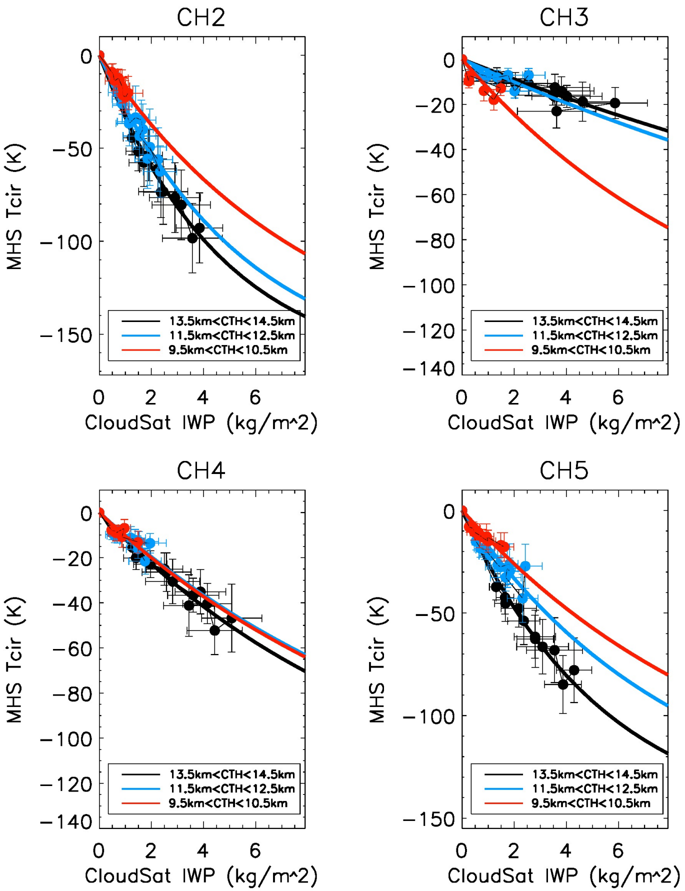

Fig. 4. PDF peaks (uncertainties given as error bars) and the corresponding regression lines based on Eqs. (2) and (4) for clouds with h_t between 13.5 and 14.5 km (black), 11.5 and 12.5 km (blue) and 9.5 and 10.5 km (red) for CH#2–CH#5 at near-nadir views.

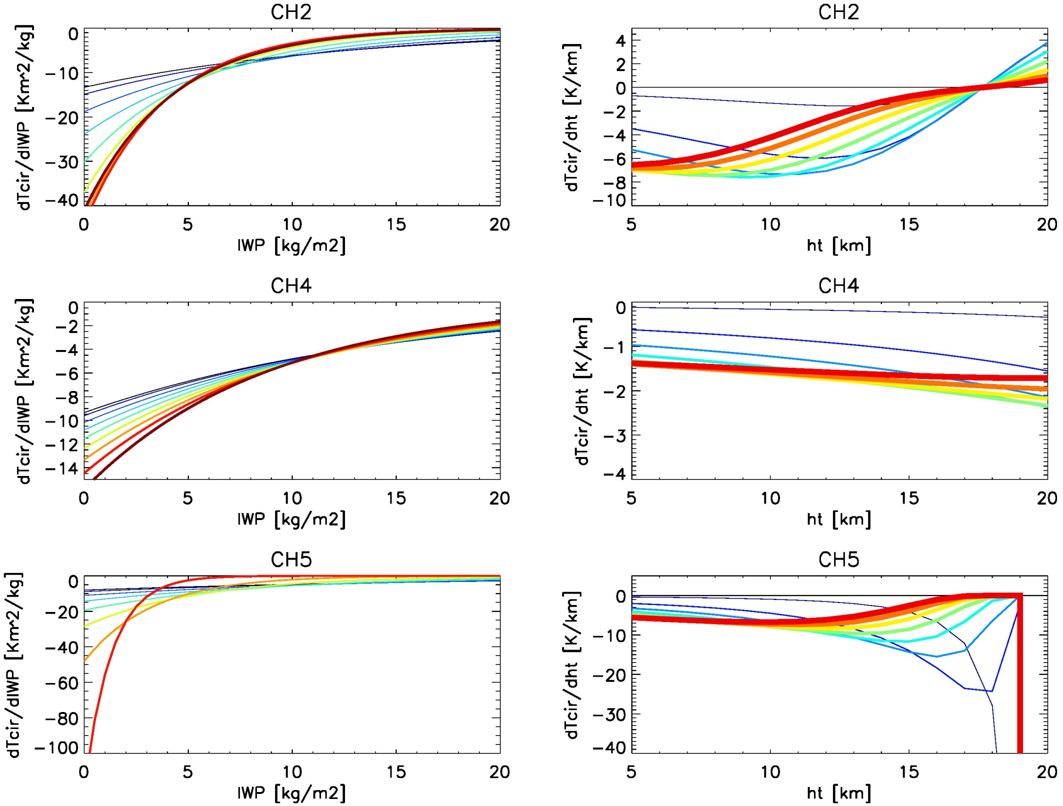

Fig. 5. Analytical solutions of the two components of the Jacobian matrix **K**: $\partial T_{\mathrm{cir}}/\partial \mathrm{IWP}$ with fixed h_t (left panels) and $\partial T_{\mathrm{cir}}/\partial h_t$ with fixed IWP (right panels). For the left column, the fixed h_t value increases fro 6 (thin, blue) to 20 km (thick, red) with an interval of 2 km. For the right column, the fixed IWP value increases from 0.5 (thin, blue) to 18 kg m^{-2} (thick, red) with an interval of 2.5 kg m^{-2}.

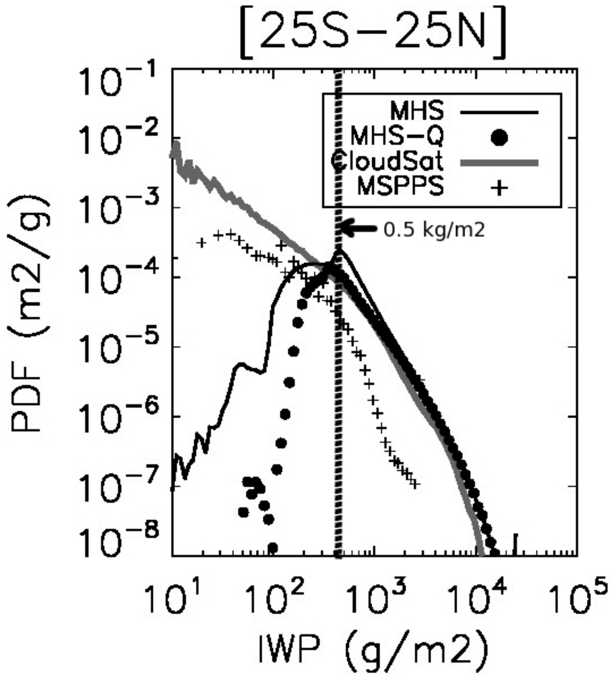

Fig. 6. PDFs of CloudSat IWP (grey thick line; smoothed over 15 CloudSat footprints and integrated between 5 and 19 km), all retrieved MHS IWP (black solid line; from all views), retrieved MHS IWP that is quality controlled (black dots), and MSPPS IWP (black crosses; from all views; from NOAA-18 only) for August 2010 in the tropics.

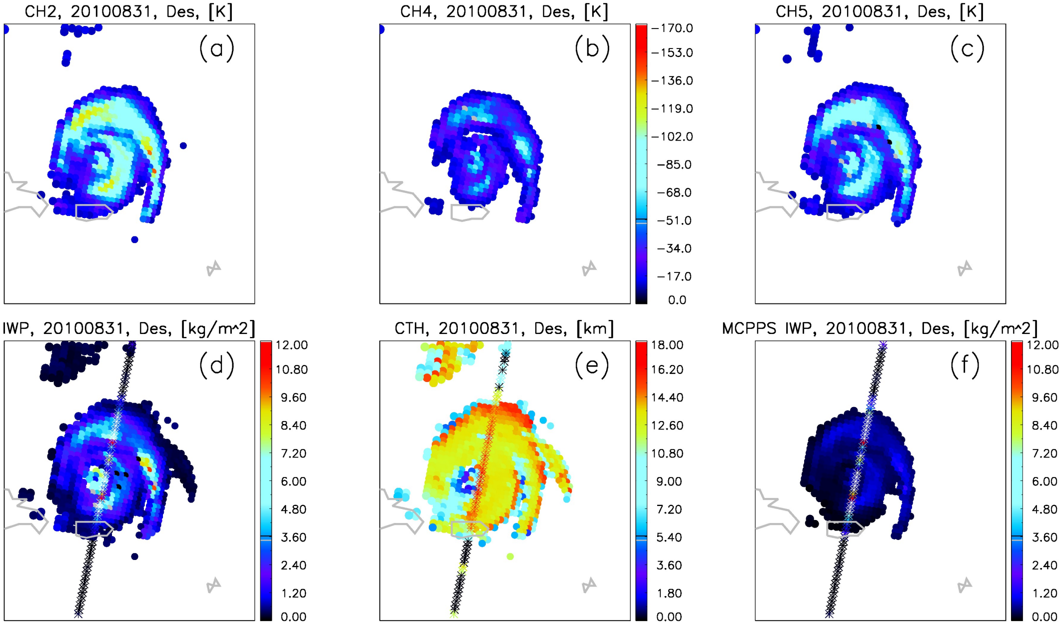

Fig. 7. T_{cir} at CH#2 **(a)**, CH#4 **(b)** and CH#5 **(c)** and retrieved NOAA-18 MHS IWP **(d)**, h_{t} **(e)** and MSPPS IWP **(f)** for Hurricane Earl at 01:54 LST on 31 August 2010 (Cuba is the island that this hurricane touched at this moment). The IWP (h_{t}) calculated from the collocated and coincident CloudSat overpass (averaged onto MHS footprints) are marked by color crosses that share the same color bars with MHS.

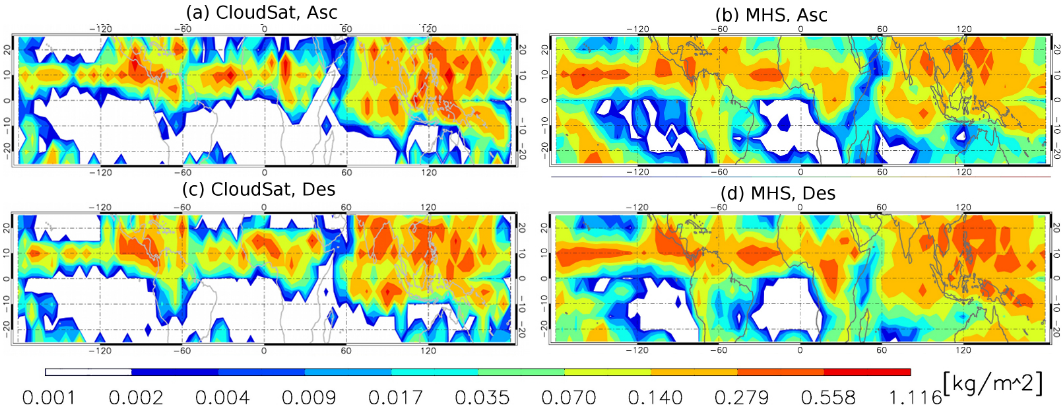

Fig. 8. Monthly averaged IWP from CloudSat and MHS ascending **(a, b)** and descending **(c, d)** orbits during August 2010. MHS IWP is averaged over all-views. Data are sampled to 5° × 5° grid boxes.

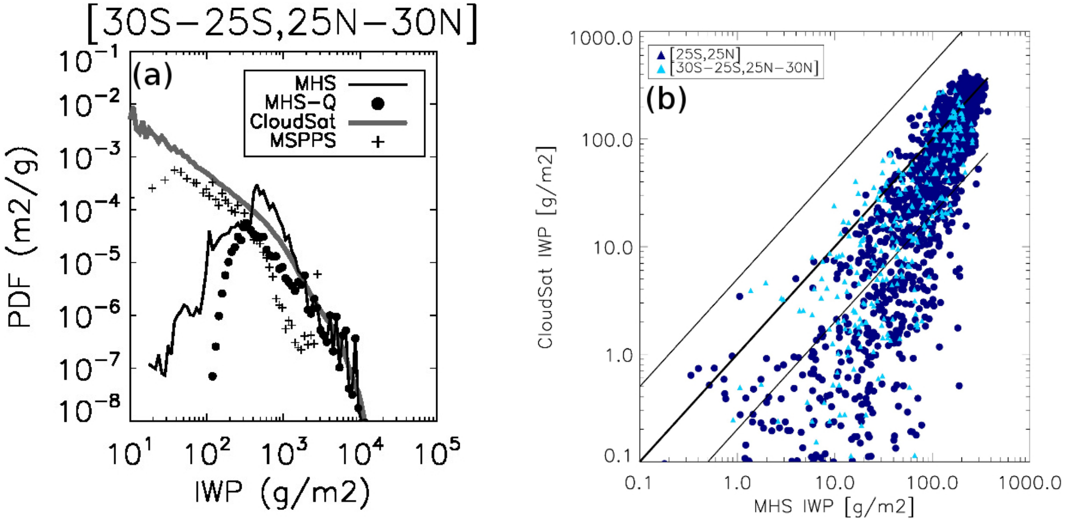

Fig. 9. (a)–(c) are the same with Fig. 6, except from different latitude bins (see sub-titles for the latitude range). (d) is the scatter plot of MHS (abscissa) and CloudSat (ordinate) gridded monthly mean IWP for latitude bins between [25° S, 25° N] (blue filled dots), [25°, 30°] N, S (light blue triangle), [30°, 50°] N, S (yellow circle), [50°, 80°] N, S (dark red circle). The map grid size is 5° × 5°, and data are then smoothed by 2-point window along latitude and longitude before making the scatter plot. The black thick (thin) line marks the 1 : 1 (1 : 5 and 5 : 1) ratio.

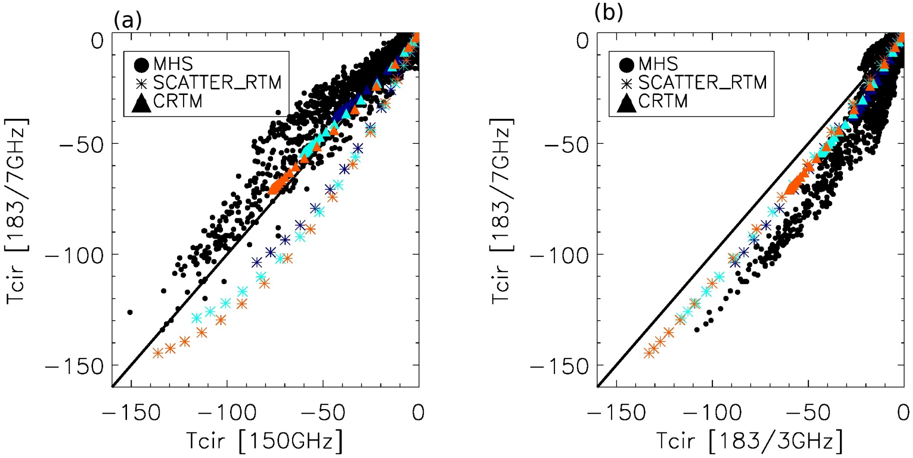

Fig. 10. Scatter plots of T_{cir} relationships between CH#2 and CH#5 **(a)**, and CH#4 and CH#5 **(b)** from observed T_{cir} at MHS nadir-view (black dots), simulated T_{cir} from CRTM (triangles) and from CRM (stars). Blue/cyan/red colors represent cloud layer with tops at 10/12/14 km and bottoms at 7.5 km in the simulations.

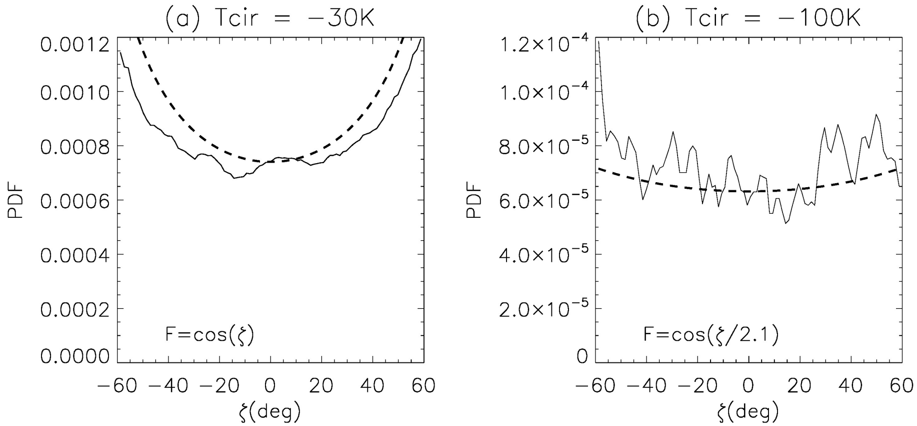

Fig. A1. PDF of T_{cir} in the range of [−100, −99 K] **(a)** and [−50, −49 K] **(b)** as a function of scan angle derived from a month of NOAA-18 MHS T_{cir} data (December 2010). Thick solid curves are calculated from the mean PDF values averaged over the 10 nadir-view FOVs divided by a factor of $\cos(\zeta/2.1)$ **(a)** and $\cos\zeta$ **(b)**, respectively, and are used to fit the observed PDF curves. ζ is the solar zenith angle.